Specific heat effects in two-dimensional shock refractions

Daniel Martínez-Ruiz[a], **César Huete**[b], **Pedro J. Martínez-Ferrer**[c], **Daniel Mira**[c]

Abstract Compressible mixtures in supersonic flows are subject to significant temperature changes via shock-waves and expansions, which affect several properties of the flow. Besides the widely-studied variable transport effects such as temperature-dependent viscosity and conductivity, vibrational and rotational molecular energy storage is also modified through the variation of the heat capacity c_p and heat capacity ratio γ, specially in hypersonic flows. Changes in the composition of the mixture may also modify its value through the species mass fraction Y_α, thereby affecting the compression capacity of the flow. Canonical configurations are studied here to explore their sharply-conditioned mechanical equilibrium under variations of these thermal models. In particular, effects of $c_p(T, Y_\alpha)$ and $\gamma(T, Y_\alpha)$ on the stability of shock-impinged supersonic shear and mixing layers is addressed, on condition that a shock wave is refracted. It is found that the limits defining regular structures are affected (usually broadened out) by the dependence of heat capacities with temperature. Theoretical and high-fidelity numerical simulations exhibit a good agreement in the prediction of regular shock reflections and their post-shock aerothermal properties.

Keywords Shock Waves · Shear Layers · Specific Heats · Thermally-perfect Gas · Hypersonic Flow

1 Introduction

Diverse technological applications involve high-speed flows, such as supersonic and hypersonic vehicles, ballistic and reentry devices, fusion by inertial confinement or detonation phenomena amongst others. Besides operating under extreme velocity conditions, large temperature variations are also characteristic of these flows, which enrich and complicate the physics and dynamics. Details on the interaction of physical processes are key to the prediction and, most important, to the understanding of these uncommon problems. In particular, high-speed propulsion devices have been studied and developed in the last decades to provide aircraft with the high requisites of thrust and endurance that characterize the aerospace sector [1–3]. To this end, various configurations are being considered to design a stable and efficient combustion chamber that can operate at a wide collection of regimes. A special distinction is given to well established concepts, such as oblique detonation wave engines (ODWE) and supersonic combustion ram jets (SCRAMJETS), where chemical reaction is promoted via compression of the fuel-air mixture. Inside these combustion devices, an intricate interplay between shocks and streams of reactants yields a stable power output. A great number of scientific studies has been performed to clarify many relevant details of this kind of compressible problems, including shock interactions with canonical turbulence [4–8], planar interactions with gaseous interfaces [9–11], shock-shock interactions [12,13], shock reflections on solid walls [14–17] and boundary-layer effects [18–22] that may include separation processes [23,24], or transmission of flow discontinuities across tangential layers [25–27], to name a few.

[a] ETSIAE, Universidad Politécnica de Madrid, Plaza del Cardenal Cisneros, 3, 28040, Madrid, Spain
[b] Grupo de Mecánica de Fluidos, Universidad Carlos III de Madrid, Av. de la Universidad 30, 28911, Leganés, Spain
[c] Barcelona Supercomputing Center, C. Jordi Girona, 29, 08034, Barcelona, Spain
Corr. author E-mail: chuete@ing.uc3m.es

The mechanical disquisitions over the equilibrium and dynamics of high-speed flows have long benefited from theoretical approximations of ideal flow [28,29] and small-perturbation methods [30,31]. In addition, further efforts to include real-flow effects have shed light on viscous processes in the related mechanics [32–36,24] as well as thermal and thermochemical non-equilibrium [37]. However, besides few studies on one-dimensional [38–40] and two dimensional waves [41], ideal-gas and calorically-perfect assumptions have been adopted in the vast majority of the analyses of compressible continuum-model fluids. These studies [38–41] focus on the effect of non-calorically-perfect gases on the structure and thickness of shock waves. Specifically, the heat capacity of the gaseous mixture is not constant and depends on the concentration of species Y_α and its temperature T. This is an interesting feature to explore not only in the formation of the shock wave structure, but also on the dynamic effects of hypersonic flows [2], considered above the value of Mach number $M > 5$, where a great increase of temperature and pressure is expected upon the formation of these waves. In particular, $c_p(T, Y_\alpha)$ and $\gamma(T, Y_\alpha)$ will be explored in this theoretical and numerical study to produce deeper insight in terms of their role to store energy and affect the compressions and expansions of the flow, thus modifying the dynamics of hypersonic streams and the impact produced on the postshock region. To the best of the authors' knowledge, the lack of literature on this aspect motivates the present study to emphasize the mechanical first-order variations that can arise in highly-energetic compressible flows upon consideration of variable specific heat capacities.

Although we recognize the valuable information that can be extracted from one-dimensional cases and shock structure studies, large corrections to the calorically-perfect scenario must be included in higher-dimension flows as noted by the experimental works on shock refractions for ideal monatomic (argon) and real diatomic (air) cases of [42], [43] and [44]. There, variations on the compressibility potential of thermally-perfect gases involve not only a dilation of the wave thickness, but also a change in the relative outcome to the tangential direction, namely the stream deflection. These post-shock pressure, temperature and deflection conditions are intimately connected and can produce real scenarios that differ from the classical, i.e., calorically perfect, flow field predictions. In order to assess their importance, a canonical configuration of compressible coflowing supersonic streams traversed by an oblique shock wave is chosen, on condition that a shock is reflected, as shown in Fig. 1. The specific problem addressed in this work aims to reduce the parametric dependence of possible multi-species supersonic flow configurations and avoid the subsonic boundary layer region in wall flows. Two parallel streams may form a shear layer if different velocity conditions are specified at the inflow, and produce a mixing layer if different thermal conditions of composition and temperature are chosen. Therefore, this enables an instructive study of thermally-perfect gas effects on the dynamics of compressible flows in a simplified configuration. This unsophisticated structure allows to introduce and conduct theoretical analyses on the modified flow conditions and, furthermore, to perform accurate numerical simulations in the absence of elaborate boundary conditions that could influence the outcomes of the analysis. The analytical formulation of the Rankine-Hugoniot equations governing the flow changes across the shocks, either incident, transmitted or reflected, allows the use of different models for the total enthalpy and is presented in terms of general parameters. The proposed model is used here to address the interaction of oblique shocks with thermally and calorically-perfect mixing layers and compare it with high-fidelity simulations. Additionally, the proposed numerical setup provides a simple benchmark to be used in compressible-flow codes that aim to reproduce shock refractions in hypersonic conditions.

For the reader's convenience, the outline of the paper is stated in the following. First, the formulation of the problem is presented in section 2, where theoretical predictions are detailed on a general basis. The implementation of accurate constitutive models of specific heat dependence with temperature and composition are also discussed in this section. The results provided by the analytical and numerical methods are presented in section 3, where regular and irregular refractions are analyzed. Later, a comprehensive discussion is presented in section 4 based on the limits of validity and the post-interaction flow. Finally, section 5 provides the main conclusions of this work. Details of the high-fidelity numerical simulations are given in section A.

2 Ideal flow formulation

The interactions of oblique shock waves with shear and mixing layers formed by two gaseous streams may result in a diverse set of configurations. The case considered in this work lies on the simplest regimes, provided
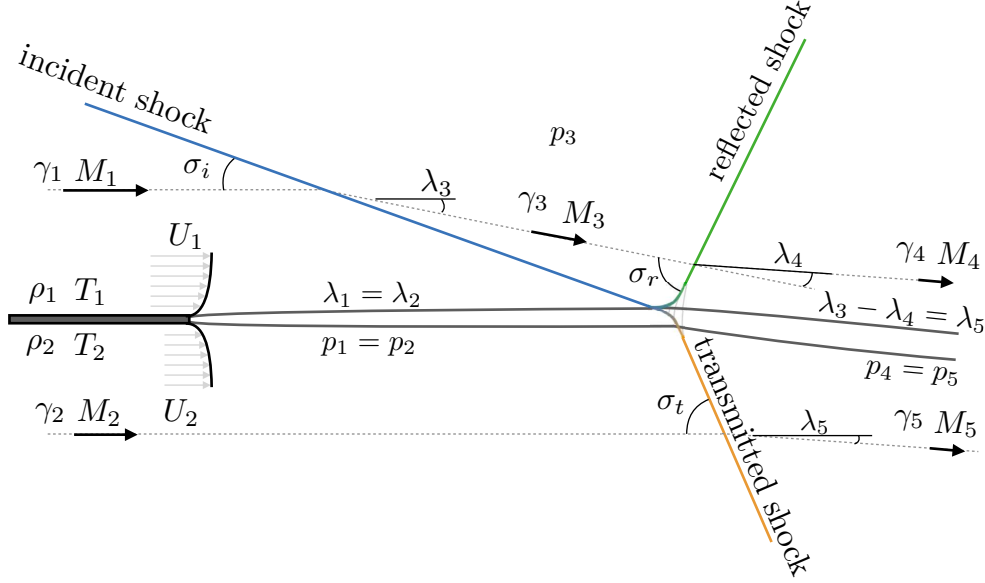
Fig. 1 Sketch of the interaction of an oblique shock impinging on two supersonic streams, where a reflected shock is produced.

that both streams are supersonic and thus rendering a transmitted oblique shock and a reflected wave. The latter may take expansive (expansion fan) or compressive (shock) character depending on the equilibrium conditions to be met downstream [25, 45–48].

Under this configuration, the steady flow field is divided into well-defined regions of homogeneous properties separated either by tangential discontinuities or waves, as sketched in Fig. 1 for a shock refraction case. In particular, ideal-flow analysis renders infinitely thin discontinuities for shocks and shear-mixing layers that separate these homogeneous regions. The emerging composition requires downstream balance of pressure $p_4 = p_5$ and deflection $\lambda_4 = \lambda_5$, for a given set of upstream Mach numbers M_1, M_2 and incident shock angle σ_i, provided that the pressure of the incoming streams equals on both sides of the contact surface, $p_1 = p_2$.

However, mechanical equilibrium may not always be achieved throughout the complete parametric space (M_1, M_2, σ_i), then impeding the possibility of an steady flow for certain combinations of their values. Specifically, the maximum pressure and deflection provided by the incident and transmitted shocks may not be sufficiently close to be matched between them through a third reflected wave. In that case, the flow evolves instead into a self-similar irregular structure that grows with time [27]. Another possibility arises when considering a subsonic flow in the lower gaseous stream, which makes the analytical treatment even more complicated. In that situation, the lower-stream region is non-uniform and, since it is subsonic, it can affect the incident shock properties upstream, see [31] for steady weak-shock interactions.

Since this work focuses on the effect of considering a non-constant specific heat $c_p(T, Y_\alpha)$, a situation that typically arises in hypersonic mixture scenarios, the aforementioned complications that may obstruct this particular analysis are avoided. Besides, to direct the study in the case where this effect is most relevant, we restrict ourselves to the reflected shock configuration, where the temperature can only increase along the streamlines. Furthermore, as the specific heat ratio variations control the jump of fluid variables across the shock wave, the parametric space of the problem must hereafter include γ, subject to the absolute temperature of the injected streams T_1, T_2, and their composition $Y_{\alpha 1}$, $Y_{\alpha 2}$, together with the values of M_1, M_2 and σ_i.

2.1 Rankine-Hugoniot relations

While the fluid particles in the upper stream undergo two sudden transformations across the incident and reflected shocks, the corresponding flow in the lower stream is only affected by the transmitted shock. Either case, for each shock passage, the corresponding conservation of mass, momentum and energy that govern

the flow variables change, namely

$$\rho_{\mathrm{u}} u_{\mathrm{u_n}} = \rho_{\mathrm{d}} u_{\mathrm{d_n}}, \tag{1}$$

$$p_{\mathrm{u}} + \rho_{\mathrm{u}} u_{\mathrm{u_n}}^2 = p_{\mathrm{d}} + \rho_{\mathrm{d}} u_{\mathrm{d_n}}^2, \tag{2}$$

$$h_{\mathrm{u}} + \frac{1}{2} u_{\mathrm{u_n}}^2 = h_{\mathrm{d}} + \frac{1}{2} u_{\mathrm{d_n}}^2, \tag{3}$$

along with the tangential velocity conservation $u_{\mathrm{u_t}} = u_{\mathrm{d_t}}$. The velocity is decomposed into the normal (n) and tangential (t) contributions relative to the shock front and the subscripts u and d are, respectively, the upstream and downstream (i.e. post-shock) values of the specified variable. The function h is the enthalpy of the gas.

When high temperature changes are expected in the flow field, the dependence of the specific heat c_p with temperature must be taken into account. This condition impedes the use of $\gamma(T, Y_\alpha) = c_p/c_v$ to define the enthalpy of the flow as $\gamma/(\gamma-1)\, p/\rho$. As a direct consequence, stagnation temperature is no longer conserved across the shock. Besides, the classical Rankine-Hugoniot equations, which typically reduce to functions of the normal component of flow Mach number and the ratio of specific heats $(M_{\mathrm{u_n}}, \gamma_{\mathrm{u}}, \gamma_{\mathrm{d}})$, can no longer be employed to predict the jump conditions. There exists, however, a simple form to circumvent this hurdle by the use of the auxiliary functions [49]

$$g = \frac{h}{h - p/\rho} \qquad \text{and} \qquad m = \frac{u_{\mathrm{n}}}{\sqrt{gp/\rho}}, \tag{4}$$

which are the reduced dimensionless enthalpy and the normal component of the velocity ahead of the shock, respectively. It is straightforward to see that $g = \gamma = \gamma_s$ in the approximation of calorically-perfect gases, $c_p = \mathrm{const.}$, where the function γ_s is associated to the dimensionless slope of the isentrope relative to the isothermal speed of sound, namely the speed of sound a, needed to define the Mach number, and which can be calculated by assuming known the equation of state $p = p(\rho, T)$ and the internal energy $\epsilon = \epsilon(c_v(T), T)$. The isentropic condition renders

$$a^2 = \left.\frac{\partial p}{\partial \rho}\right|_s = \gamma_s \frac{p}{\rho} = \frac{\left.\frac{\partial p}{\partial T}\right|_\rho}{\left.\frac{\partial \epsilon}{\partial T}\right|_\rho} \frac{p}{\rho^2} + \left.\frac{\partial p}{\partial \rho}\right|_T - \frac{\left.\frac{\partial p}{\partial T}\right|_\rho \left.\frac{\partial \epsilon}{\partial \rho}\right|_T}{\left.\frac{\partial \epsilon}{\partial T}\right|_\rho} = \frac{c_p}{c_v} R_g T \tag{5}$$

that equals $\gamma_s = \gamma$ upon thermal equilibrium. The auxiliary function m_{u} relates to the upstream Mach number through $M_{\mathrm{u_n}} = M_{\mathrm{u}} \sin\sigma = m_{\mathrm{u}} \sqrt{\gamma_{\mathrm{u}}/g_{\mathrm{u}}}$. Therefore, Rankine-Hugoniot conservation conditions across a shock jump for a gas that is not calorically perfect can be rewritten with use made of the above-mentioned coefficients. The mass-compression ratio reads

$$\mathcal{R} = \frac{\rho_{\mathrm{d}}}{\rho_{\mathrm{u}}} = \frac{g_{\mathrm{d}}(g_{\mathrm{u}} - 1)(1 + g_{\mathrm{u}} m_{\mathrm{u}}^2)}{g_{\mathrm{u}}(g_{\mathrm{d}} - 1)\left[2 + (g_{\mathrm{u}} - 1)m_{\mathrm{u}}^2\right]} +$$
$$+ \frac{\sqrt{g_{\mathrm{u}} - 1}\sqrt{g_{\mathrm{u}}^2 m_{\mathrm{u}}^2\left[2 + (g_{\mathrm{u}} - 1)m_{\mathrm{u}}^2\right] - g_{\mathrm{d}}^2\left[2 g_{\mathrm{u}} m_{\mathrm{u}}^2 - g_{\mathrm{u}} + 1\right]}}{g_{\mathrm{u}}(g_{\mathrm{d}} - 1)\left[2 + (g_{\mathrm{u}} - 1)m_{\mathrm{u}}^2\right]}, \tag{6}$$

from which it follows that the pressure and temperature increase across the shock is

$$\mathcal{P} = \frac{p_{\mathrm{d}}}{p_{\mathrm{u}}} = 1 + g_{\mathrm{u}} m_{\mathrm{u}}^2 \sin^2\sigma (1 - \mathcal{R}^{-1}) \qquad \text{and} \qquad \mathcal{T} = \frac{T_{\mathrm{d}}}{T_{\mathrm{u}}} = \frac{\mathcal{P}}{\mathcal{R}}. \tag{7}$$

The compressed gas leaves the oblique shock following a deflected angle λ with respect to the upstream flow direction and a Mach number $M_{\mathrm{d_n}} = M_{\mathrm{d}} \sin(\sigma - \lambda) = m_{\mathrm{d}} \sqrt{\gamma_{\mathrm{d}}/g_{\mathrm{d}}}$, given respectively by the functions

$$\lambda = \sigma - \tan^{-1}\left(\frac{\tan\sigma}{\mathcal{R}}\right) \quad \text{and} \quad m_{\mathrm{d}} = \sqrt{\frac{g_{\mathrm{u}}}{g_{\mathrm{d}} \mathcal{P} \mathcal{R}}} m_{\mathrm{u}}. \tag{8}$$

The jump conditions above are employed to write the system of equations that describe the three-shock structure. For given values of m_1, g_1 and σ_{i}, direct evaluation of these expressions provides

$$\lambda_3 = \lambda(m_1, \sigma_{\mathrm{i}}, g_1, g_3) \quad \text{and} \quad p_3 = p_1 \mathcal{P}(m_1, \sigma_{\mathrm{i}}, g_1, g_3) = p_1 \mathcal{P}_{\mathrm{i}}, \tag{9}$$

$$m_3 = m_d(m_1, \sigma_i, g_1, g_3) \quad \text{and} \quad T_3 = T_1 \mathcal{T}(m_1, \sigma_i, g_1, g_3) = T_1 \mathcal{T}_i. \tag{10}$$

Flow properties behind the incident shock can be obtained by providing the constitutive expression of the specific heat $c_p(T, Y_\alpha)$, which depends on the upper-stream fluid species Y_1 and the absolute temperature T_3. For thermally-perfect gases, the specific heat ratio and the enthalpy coefficient can be written as functions of the upper-stream specific heat capacity $c_{p_1}(T_3)$ and the specific gas constant R_{g_1}, namely

$$g_3 = \frac{h(T_3)}{h(T_3) - p_3/\rho_3} = \frac{h_{1_f} + h_{1_{\text{ref}}} + \int_{T_{\text{ref}}}^{T_3} c_{p_1}(T)\mathrm{d}T}{h_{1_f} + h_{1_{\text{ref}}} + \int_{T_{\text{ref}}}^{T_3} c_{p_1}(T)\mathrm{d}T - R_{g_1}T_3}, \tag{11}$$

where the subindex f indicates the formation enthalpy of the species in the upper stream and ref is used for standard reference conditions at $T_{\text{ref}} = 298.15$ K. This expression, along with (10), renders an implicit relation for T_3 that finally provides g_3 and the rest of the flow properties. Likewise, the value of the flow Mach number can be easily deduced with $M_3 \sin(\sigma_i - \lambda_3) = m_3 \sqrt{\gamma_3/g_3}$. In an analogous manner, equations

$$\lambda_5 = \lambda(m_2, \sigma_t, g_2, g_5) \quad \text{and} \quad p_5 = p_1 \mathcal{P}(m_2, \sigma_t, g_2, g_5) = p_1 \mathcal{P}_r, \tag{12}$$

$$m_5 = m_d(m_2, \sigma_t, g_2, g_5) \quad \text{and} \quad T_5 = T_2 \mathcal{T}(m_2, \sigma_t, g_2, g_5) = T_2 \mathcal{T}_t, \tag{13}$$

yield the downstream flow properties below the transmitted shock, involving the unknown values of the transmitted-shock angle σ_t and the enthalpy coefficient g_5. Assuming also a thermally perfect gas, the specific heat ratio and enthalpy coefficient will be given by the lower-stream component Y_2 properties,

$$g_5 = \frac{h(T_5)}{h(T_5) - p_5/\rho_5} = \frac{h_{2_f} + h_{2_{\text{ref}}} + \int_{T_{\text{ref}}}^{T_5} c_{p_2}(T)\mathrm{d}T}{h_{2_f} + h_{2_{\text{ref}}} + \int_{T_{\text{ref}}}^{T_5} c_{p_2}(T)\mathrm{d}T - R_{g_2}T_5}. \tag{14}$$

On the other hand, expressions providing the jump conditions between region-3 and region-4 can be directly presented with the expressions

$$\lambda_4 = \lambda(m_3, \sigma_4, g_3, g_4) \quad \text{and} \quad p_4 = p_3 \mathcal{P}(m_3, \sigma_4, g_3, g_4) = p_3 \mathcal{P}_r, \tag{15}$$

$$m_4 = m_d(m_3, \sigma_4, g_3, g_4) \quad \text{and} \quad T_4 = T_3 \mathcal{T}(m_3, \sigma_4, g_3, g_4) = T_3 \mathcal{T}_r, \tag{16}$$

which must apply to the upper-stream flow properties above the contact surface, where

$$g_4 = \frac{h(T_4)}{h(T_4) - p_4/\rho_4} = \frac{h_{1_f} + h_{1_{\text{ref}}} + \int_{T_{\text{ref}}}^{T_4} c_{p_1}(T)\mathrm{d}T}{h_{1_f} + h_{1_{\text{ref}}} + \int_{T_{\text{ref}}}^{T_4} c_{p_1}(T)\mathrm{d}T - R_{g_1}T_4}. \tag{17}$$

Finally, the two additional mechanical equilibrium conditions to be imposed at the downstream contact-surface read,

$$p_5 = p_4 \quad \text{and} \quad \lambda_5 = \lambda_3 - \lambda_4, \tag{18}$$

i.e., all streamlines are parallel again with equal deflection angle and pressure. Equations (9)-(18) provide a set of seventeen algebraic equations that determine m_3, m_4, m_5, σ_r, σ_t, λ_3, λ_4, λ_5, p_3/p_1, p_4/p_1, p_5/p_1, T_3, T_4, T_5, g_3, g_4 and g_5. The Mach numbers of the downstream flow are given by $M_4 \sin(\sigma_r - \lambda_4) = m_4 \sqrt{\gamma_4/g_4}$ and $M_5 \sin(\sigma_t - \lambda_5) = m_5 \sqrt{\gamma_5/g_5}$ for the upper and lower streams, respectively. Considering the latter as playing the role of an additional specific heat ratio $g_i \simeq \gamma_i$, in the form $g(T, Y_\alpha)$, calls for six more equations than the calorically-perfect case, where direct identification yields exact equivalence between the specific heat ratio and enthalpy coefficient $g = \gamma = $constant.

Although the non-linear system described above must be solved numerically, due to the trigonometric and implicit relationships involved, a qualitative description of the variable specific heat ratio can be withdrawn with use made of the well-known polar Henderson-Neumann diagrams [25,27]. First, each curve shown in Fig. 2 (a) is the combination of possible outcomes in terms of deflection λ and pressure jump p_d/p_u, namely the hodograph plane, of a shock wave for a given upstream Mach number and specific heat ratio. The curve is the collection of points for all the possible shock angles σ ranging from 0 to 180 degrees. In particular, the incident-shock polar is drawn in blue for fixed values of M_1, $\gamma_1(= g_1)$, and a specific shock angle σ_i is marked with a blue circle, providing post-shock deflection and pressure. In addition, departing from these
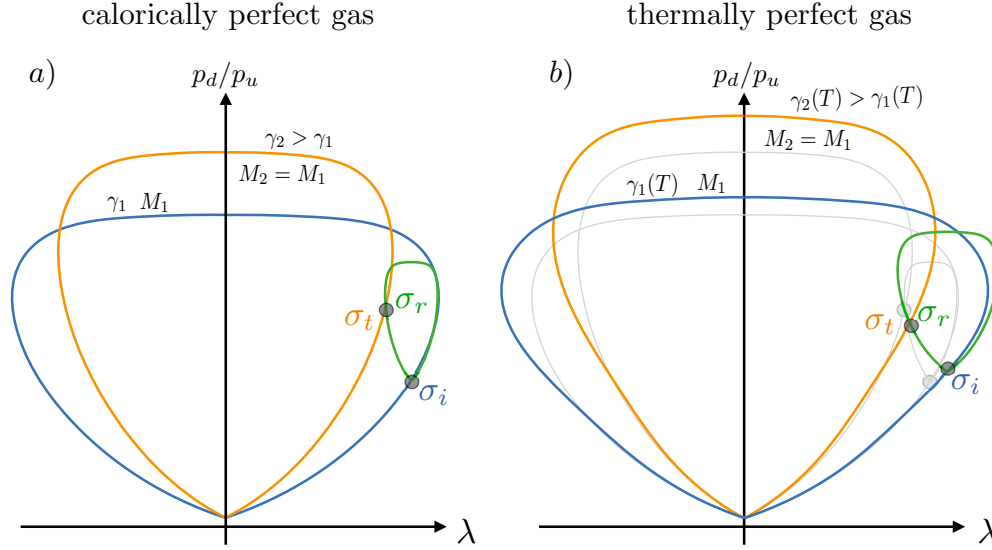
Fig. 2 Qualitative effect on the polar diagram $p_\mathrm{d}/p_\mathrm{u}$-$\lambda$ when considering constant specific heat, with $g = \gamma$ (a), or variable specific heat with $g(T) \neq \gamma(T)$ (b).

conditions one can represent the reflected-shock polar in green for a Mach number M_3, which must render conditions compatible with the lower-stream polar. The latter is drawn in orange for upstream conditions $M_2 = M_1$, and $\gamma_2 > \gamma_1$. The intersection between the two provides implicitly the angles of the lower-stream transmitted shock σ_t and upper-stream reflected shock σ_r, and explicitly equilibrium downstream conditions $\lambda_4 = \lambda_5$, $p_4 = p_5$. Therefore, a coflow of two streams with equal Mach number and different specific heat ratio traversed by an oblique shock produces a refraction easily described by the angles obtained in the polar diagram.

A particular behavior is expected for different combinations of M_1, M_2 and σ_i, such that the intersecting point in the hodograph plane σ_t becomes tangential. The latter will be here considered as the critical case for regular refractions and further variations would readily provide a mismatch that lacks analytical solution with a combination of three straight shocks. The actual structure arising in such a case involves a complex set of irregular discontinuities that has already been shown to grow self-similarly over time [27]. In that way, for a given upstream condition M_1 and σ_i, there is an upper M_{2c}^{+} and a lower critical value M_{2c}^{-} that produce pseudo-steady irregular refractions.

Moreover, thermally-perfect conditions have been shown to modify the shock relations. Anticipating that $g(T)$ decreases monotonically with temperature, the polar diagrams evolve as shown in Fig. 2 (b) with $\gamma(T)$ and $g(T)$. For the same Mach number M and shock angle σ (thus same intensity of the shock $M_n = M \sin\sigma$), both the flow deflection and the pressure jump increase with respect to the calorically-perfect case, thus modifying the critical values $M_{2c}^{\pm}$ expected under constant γ analyses. It should be noted that each point of the polar, be different shock angle, provides a different post-shock temperature and, thus, $\gamma(T)$ and $g(T)$ values. In addition, a decrease of the latter directly involves a greater capability of deflecting the flow and generating overpressure as denoted by the enlarged polar shapes. This effect of variable specific heat ratio is readily seen from the energy conservation equation, conveniently written as

$$\frac{g_\mathrm{u}}{g_\mathrm{u} - 1} + \frac{1}{2} g_\mathrm{u} m_\mathrm{u}^2 = \mathcal{T} \left[\frac{g_\mathrm{u}}{g_\mathrm{u} - 1} + \frac{1}{2} g_\mathrm{d} m_\mathrm{d}^2 \right] + \mathcal{T} \frac{(g_\mathrm{u} - g_\mathrm{d})}{(g_\mathrm{u} - 1)(g_\mathrm{d} - 1)}, \tag{19}$$

which shows that an enthalpy-coefficient variation is equivalent to a temperature-dependent endothermic contribution when $g_\mathrm{u} > g_\mathrm{d}$ (exothermic when $g_\mathrm{u} < g_\mathrm{d}$). As the term on the right hand side is proportional to $\mathcal{T}$, even bounded variations in the specific heat ratio makes the contribution more noticeable as the shock intensity increases. For the case considered here, where the dissociation degree of the molecules is expected to be low and the corresponding dissociation energy is neglected in (19), the function $\gamma(T)$ can be taken as a monotonically decreasing function of temperature. Consequently, for some given values of M_u and σ,

the mass compression ratio of the fluid particles across the shock will be enhanced, along with the pressure jump and deflection angles that increase, as commented before. Keeping that in mind, when the shock is imposed by a wedge-like boundary condition (λ determined), the corresponding shock angle σ will be larger for $g_\mathrm{u} > g_\mathrm{d}$, provided that the weak (attached) solution is the valid one.

2.2 Thermally-perfect mixtures

The outlook of the compressible problem under study calls for an adequate description of the medium constitution. Consideration of thermally-perfect (also called semi-perfect) or calorically-perfect (constant heat capacity) gases, for which an ideal gas equation of state holds, is the pivotal point of the study. In order to provide an accurate behavior of the thermodynamic processes, fifth-order JANAF polynominals [50] are employed for the specific heat at constant pressure of a given species α, namely

$$c_{p\alpha}(T) = \frac{R}{W_\alpha} \left(a_{1\alpha} + a_{2\alpha}T + a_{3\alpha}T^2 + a_{4\alpha}T^3 + a_{5\alpha}T^4 \right), \tag{20}$$

in J/(kg K) units, where $R = 8.31451$ J/mol K is the universal gas constant and W_α is the molar mass of the corresponding species. The enthalpy of each species can be calculated upon integration in temperature

$$h_\alpha(T) = \frac{R}{W_\alpha} \left(a_{6\alpha} + a_{1\alpha}T + \frac{a_{2\alpha}}{2}T^2 + \frac{a_{3\alpha}}{3}T^3 + \frac{a_{4\alpha}}{4}T^4 + \frac{a_{5\alpha}}{5}T^5 \right), \tag{21}$$

where the coefficients $a_{i\alpha}$ can be found in JANAF tables. Additionally, the mixture-related specific heat and enthalpy are simply derived from weighted summation

$$c_p(T, Y_\alpha) = \sum_{\alpha=1}^{N} c_{p\alpha}Y_\alpha \quad \text{and} \quad h(T, Y_\alpha) = \sum_{\alpha=1}^{N} h_\alpha Y_\alpha. \tag{22}$$

Finally, the expression for the ratio of specific heats of the mixture including composition and temperature variation effects, is given by

$$\gamma(T, Y_\alpha) = \left(1 - \frac{R}{c_p W} \right)^{-1}, \tag{23}$$

where

$$W = \sum_{\alpha=1}^{N} X_\alpha W_\alpha = \left(\sum_{\alpha=1}^{N} \frac{Y_\alpha}{W_\alpha} \right)^{-1} \tag{24}$$

is the molar mass of the mixture, which is derived from the corresponding molar or mass fractions, X_α or Y_α respectively. As an example, Fig. 3 shows the values of the specific heat ratio γ and reduced dimensionless enthalpy g for pure streams of air, ethane (C_2H_6) and propane (C_3H_8) as a function of temperature. The sample species have been selected to explore the effects in the range of $\gamma \in (1, 1.4)$. Figure 3 also shows the initial conditions that will be later employed in the theoretical and numerical analyses (solid circles). Different pos-tshock values are selected to get an easy picture of the range of expected values, where the contraction of the temperature domain can be identified as γ approaches unity (hot C_3H_8), since temperature grows as $\mathcal{T} \sim (\gamma - 1)M_{\mathrm{u_n}}^2$ for $M_{\mathrm{u_n}} \gg 1$. The g function associated to each substance is also calculated within the same temperature range. As expected, the crossing point between this function and the ratio of specific heats occurs at $g(T_\mathrm{ref}) = \gamma(T_\mathrm{ref})$.

Additionally, particular cases of calorically-perfect gases can be included to evaluate the divergence of results. Multi-species gaseous mixtures featuring constant thermodynamic coefficients, and thus a constant specific heat ratio γ, can be easily reproduced by evaluating (20) at a desired temperature to retrieve a constant value of $c_{p\alpha}$. The corresponding enthalpy is simply evaluated via $h_\alpha = \Delta h_{\mathrm{f}\alpha}^0 + c_{p\alpha}(T - T_\mathrm{ref})$ where $\Delta h_{\mathrm{f}\alpha}^0 = h_\alpha(T_\mathrm{ref})$, $c_{p\alpha}$ and T_ref appear as constant parameters. Finally, mixture-averaged values of these quantities are obtained by simple weighted summation as described in eq. (22).
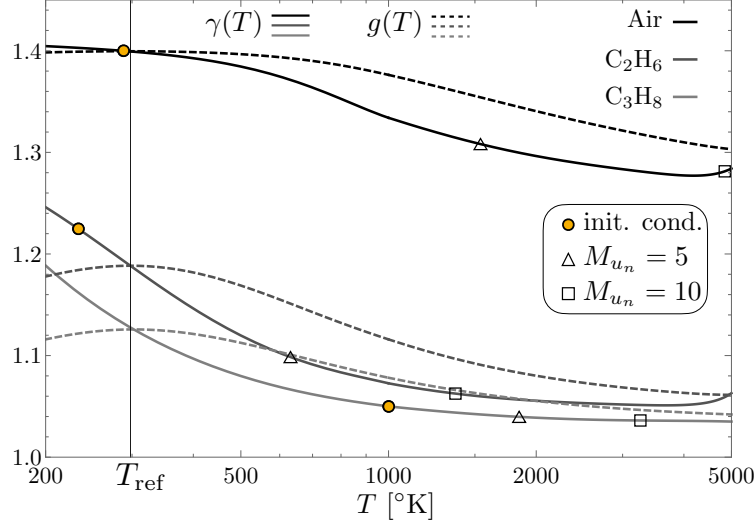
Fig. 3 Calculated values of functions $\gamma(T)$ and $g(T)$ for different species studied in this work. Circles indicate the pre-shock initial conditions used in the computations, whilst triangles and squares indicate the post-shock values of γ at different shock intensities.

3 Results for thermally-perfect and calorically-perfect flows

In this section, theoretical results accompanied by numerical simulations are shown for a variety of coflows that are the result of the coupling of flow dynamics with thermodynamics. The particular benchmark that permits the assessment of the specific heat ratio influence, representative of Fig. 1, is composed of an upper stream at Mach number $M_1 = 5$ before the incident oblique shock, which traverses the domain with an angle $\sigma_i = 60°$, and a lower stream at higher Mach number value $M_2 > M_1$. The composition and temperature is kept constant in the lower stream such that $\gamma_2 = \gamma_{air}$ and varied on the upper stream with ratios of specific heats $\gamma_1 \leq \gamma_2$. This election guarantees the reflected wave to always be an oblique shock, and therefore, larger temperature variations than those expected for the reciprocal expansion-wave reflections, which are not treated here. Consequently, the effect of $c_p(T, Y_\alpha)$, and thus $\gamma(T, Y_\alpha)$, is expected to have a greater impact under the selected combination of parameters. The solutions to the analytical problem formulated in Sec. 2 are here reproduced via numerical simulations with good agreement. These computations have been conducted including variable and constant γ, in absence of momentum, thermal or mass diffusivities (i.e., Euler equations) thus providing a direct comparison with previous results.

3.1 Numerical simulations

The problem described above is addressed with the computational fluid dynamics code CREAMS [51], which solves the compressible Navier-Stokes equations with species transport using a spatial seventh-order accurate WENO scheme and a third-order total variation diminishing Runge-Kutta scheme. These computations assist the theoretical analysis in the hodograph plane providing the otherwise unfeasible description of time-dependent responses, characterization of lengths of the generated Mach stems, and determination of the final flow-field structures in irregular scenarios. Additional details of the modelling and numerical approaches proposed for this study are given in appendix A.

3.2 Regular refractions

Three different cases associated to the specific heat ratio properties of the upper stream γ_1 are chosen to represent a variety of conditions. In particular, ambient air $\gamma_{air}(T_1 = 288.15\text{K}) = 1.4$, cold ethane $\gamma_{C_2H_6}(T_1 = 233.15\text{K}) = 1.225$, and hot propane $\gamma_{C_3H_8}(T_1 = 1000\text{K}) = 1.05$ for $M_2 \in (5, 10)$. The resolution of the 17

non-linear algebraic equations must consider that the lowest-energy solution is the one actually occurring, while the others are discarded. The calculations have been conducted including variable and constant γ.
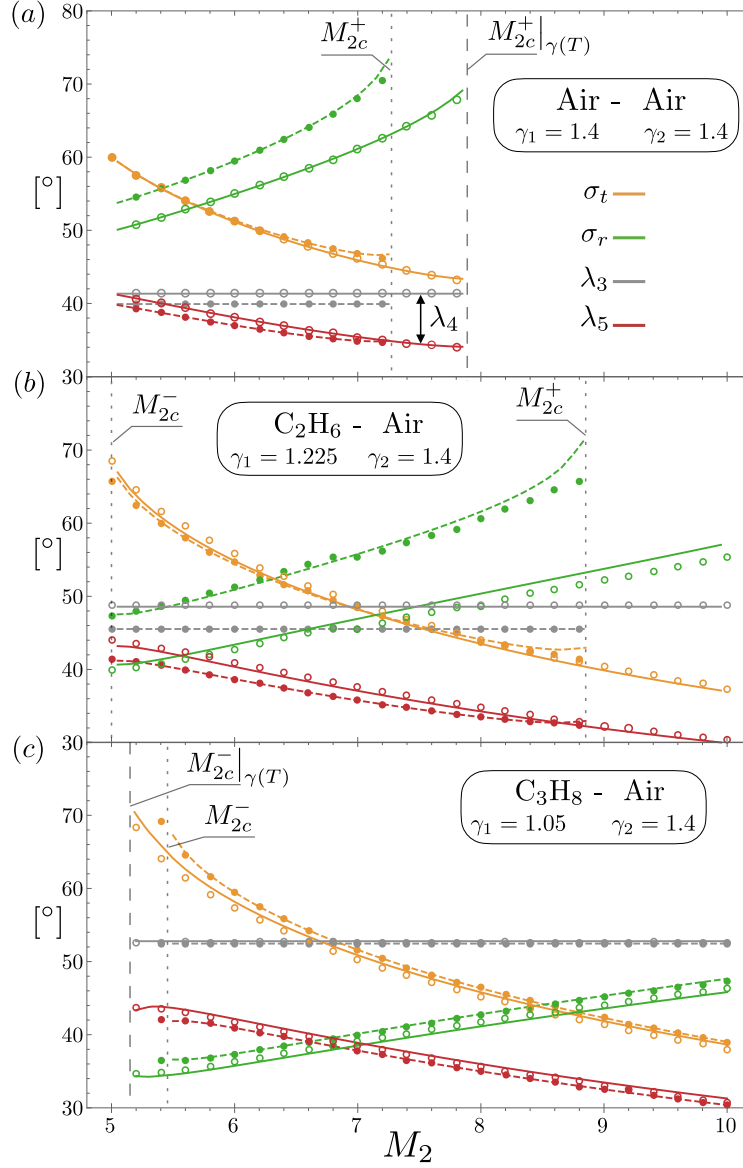

Fig. 4 Values of the problem-defining angles for $M_1 = 5$ and varying $M_2 > M_1$, for three different cases regarding composition of the upper stream. Solid lines refer to $\gamma(T)$ and dashed lines to $\gamma = \text{const}$. Empty and filled circles refer to numerical results for $\gamma(T)$ and $\gamma = \text{const.}$, respectively.

In the ideal configuration proposed in this work, where the mixing-layer thickness is negligible, the impinging oblique shock is completely straight, and upstream flows are uniform at each side of the mixing layer. This problem lacks of spatial scales and the flow field can be fully characterized by the corresponding angles. In particular, those associated to the fluid particles λ_3 and $\lambda_4 = \lambda_5$, and those related to the shocks σ_i (incident), σ_t (transmitted) and σ_r (reflected). They are plotted in Fig. 4 as a function of the Mach number of the lower stream M_2. Theoretical (solid lines) and numerical (empty circles) computations for thermally-perfect gases are displayed together showing very good agreement. Additionally, theoretical (dashed lines) and numerical simulation (filled circles) results of calorically-perfect cases are included for comparison.

Figure 4 (a) shows the resulting angles for air-air shear layers and differences are easily recognized. Firstly, the angles characterizing the upper stream (λ_3 and σ_r) are significantly changed from constant to variable specific heat ratio. The diminishing of the specific heat ratio increases the deflection capacity λ_3 of the incident oblique shock, which places the solid-gray line always over the dashed-gray line. Clearly, the values of λ_3 are not affected by the lower stream Mach number since they are fully determined by the incident shock angle, which is kept constant. On the other hand, the reflected shock angle, measured relative to the already-deflected flow ahead, is reduced. As a result, the angles describing the equilibrium with the lower stream (λ_4 and σ_t) are barely affected. Furthermore, while $M_2 > M_{2c}^+ = 7.3$ renders a pseudo-steady irregular refraction [27] when $\gamma_1 = \gamma_2 = 1.4 = \text{const.}$ (for $M_1 = 5$ and $\sigma_i = 60°$), the domain associated to regular refractions is enlarged up to $M_2 > M_{2c}^+ = 7.9$ when admitting variations in the specific heat. It should be noted that $M_2 = M_1$ renders a unique stream of air where $\sigma_t = \sigma_i$, $\lambda_5 = \lambda_3$ and $\lambda_4 = 0$, such that the reflected shock becomes a Mach line and σ_r equals the angle of the characteristics defined by $\sin^{-1}(1/M_3)$. Moreover, for iso-mixture streams, $M_2 < M_1$ configurations replace the reflected-shock for a reflected expansion, a case omitted here for the sake of conciseness.
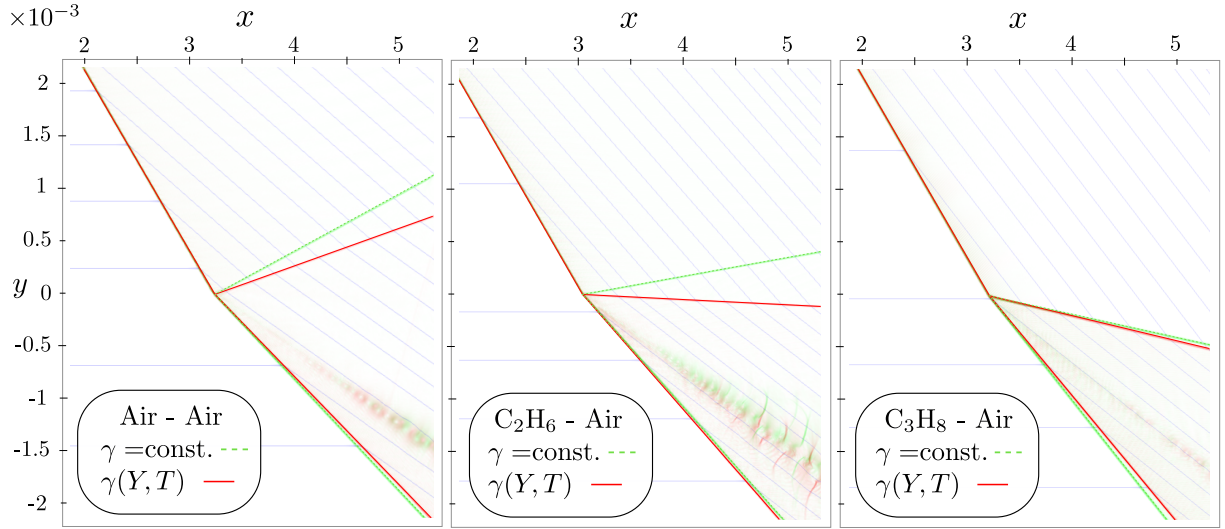

Fig. 5 Regular configurations obtained from numerical simulations of air-air, low-temperature ethane-air and hot propane-air. Superimposed results are shown for $\gamma(T, Y_\alpha)$ (red) and $\gamma = \text{const.}$ (green).

The qualitative picture of the angles characterizing the upper stream does not change when modifying its composition, thus the function $\gamma_1(T)$. This is readily seen from panels (b) and (c), which display the same functions for cold ethane-air ($\gamma_1 = \gamma_{C_2H_6}$) and hot propane-air ($\gamma_1 = \gamma_{C_3H_8}$), respectively. By way of contrast, the angles describing the lower stream are affected differently, even if both cases satisfy $\gamma_1 < \gamma_2$. For low-temperature ethane, the transmitted shock angle and the lower stream deflection are amplified when considering $\gamma(T)$, while the opposite is true for preheated propane. Regarding the origin of irregular reflections, the limit M_{2c}^+ on the right side is seen to increase for the two cases, in consonance with the air-air upper panel. Likewise, for $\gamma_1 < \gamma_2$ there exists another limit on the left side of the figure $M_{2c}^- \sim M_1$. If the value of γ is assumed constant, theory predicts that $M_2 = M_1$ is stable for ethane and unstable for hot propane (no regular solution, see Fig. 4 (c)). However, when the ratio of specific heats is adequately modelled the irregular refraction transition occurs at lower values of the lower stream Mach number M_{2c}^-. Unlike the air-air case, $M_2 < M_1$ does not necessarily produce a reflected expansion wave, since the deflection of the transmitted shock in air (represented by orange polars in Fig. 2) is smaller than that produced by the upper streams (blue polars), so that the only matching solution is provided by reflected shocks that rise up the stream (green polars). An expansion emerging from the incident shock conditions would amplify the deflection and lower the pressure, moving away from an intersecting solution.

The results of the numerical simulations of the three cases selected above are shown in Fig. 5 for comparison. The cases are set with a tangential discontinuity between streams placed at $y = 0$. Streamlines (marked in grey and corresponding to $\gamma(T, Y_\alpha)$) show their initial horizontal path and later deflection upon passage through the shocks. The shock positions are obtained from the calculation of gradients of the flow variables, mainly the flow Mach number, and are shown in red. Shocks arising from equivalent calorically perfect simulations are superimposed in green for comparison. As described above, the lower-stream angles remain nearly unaltered while larger deviations are found in the reflected shock and upper-stream deflection angles. These variations call for caution when modelling compressibility effects in high-speed flows, as the design of hypersonic devices require accurate prediction of shock positions and reflections to adapt the flow and generate the desired thrust or drag.

3.3 Irregular refractions

The analytical results displayed in Fig. 4 for the flow angles show a well-limited domain for the regular structures, which is different for thermally-perfect and calorically perfect cases. Outside that domain, the result is a self-similar pseudo-steady structure of shocks that grows moving upstream at constant speed [27]. In particular, the impingement of an oblique shock of $\sigma_i = 60°$ on the air-air coflow when moving at $M_1 = 5$ and $M_2 = 9 > M_{2c}^+$ yields an irregular shock refraction with no solution in the parametric space of Fig. 4 (a). Nevertheless, downstream conditions of the upper and lower streams can be represented in Fig. 6 (a), although no equilibrium can be met as the green and orange polars do not intersect.
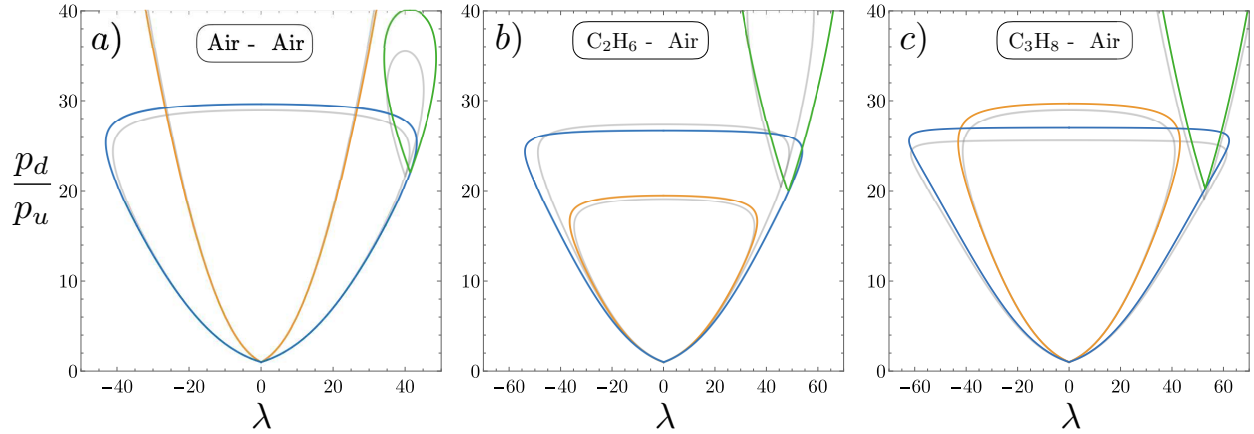

Fig. 6 Polar plots under irregular refraction conditions for $M_1 = 5$ and $\sigma_i = 60°$ for the following cases: (a) air-air with $M_2 = 9$ (b) C_2H_6-air with $M_2 = 4$ and (c) C_3H_8-air with $M_2 = 5$. Blue, orange and green loops correspond to M_1, M_2 and M_3, respectively. In light gray color is plotted the equivalent calorically-perfect solution.

Further consideration of irregular structures for $M_2 \leq M_1$ is shown in Fig. 6 (b) and (c). For example, when considering a variable heat capacity for the gas, a coflow comprising low temperature C_2H_6 (upper stream) and air (lower stream) at $M_1 = 5$, $M_2 = 4 < M_{2c}^-$ does not render a regular solution under an oblique shock of $\sigma_i = 60°$. Unlike the previous case, the blue loop does not intersect the orange one at any point, as seen in Fig. 6 (b), thus impeding the formation of a single Mach-stem structure as in the precedent case. Furthermore, when considering high-temperature C_3H_8 (upper stream) and air (lower stream) at $M_1 = 5$, $M_2 = 5 < M_{2c}^-$, the lack of intersection between the green and orange curves also translates into the formation of an irregular structure. Although $M_2 = M_1$, this case resembles the air-air coflow with $M_2 > M_1$, since the orange loop does intersect the blue one. Nevertheless, this intersection of polars provides the conditions produced behind the leading waves, which are unbalanced with the reflected-shock pressure and deflection. This intersection in Fig. 6 (a) is produced in the lower part of the M_2 polar (yielding supersonic postshock conditions in the transmitted wave), while in Fig. 6 (c) the intersection is found in the upper part of the M_2 polar (subsonic conditions).
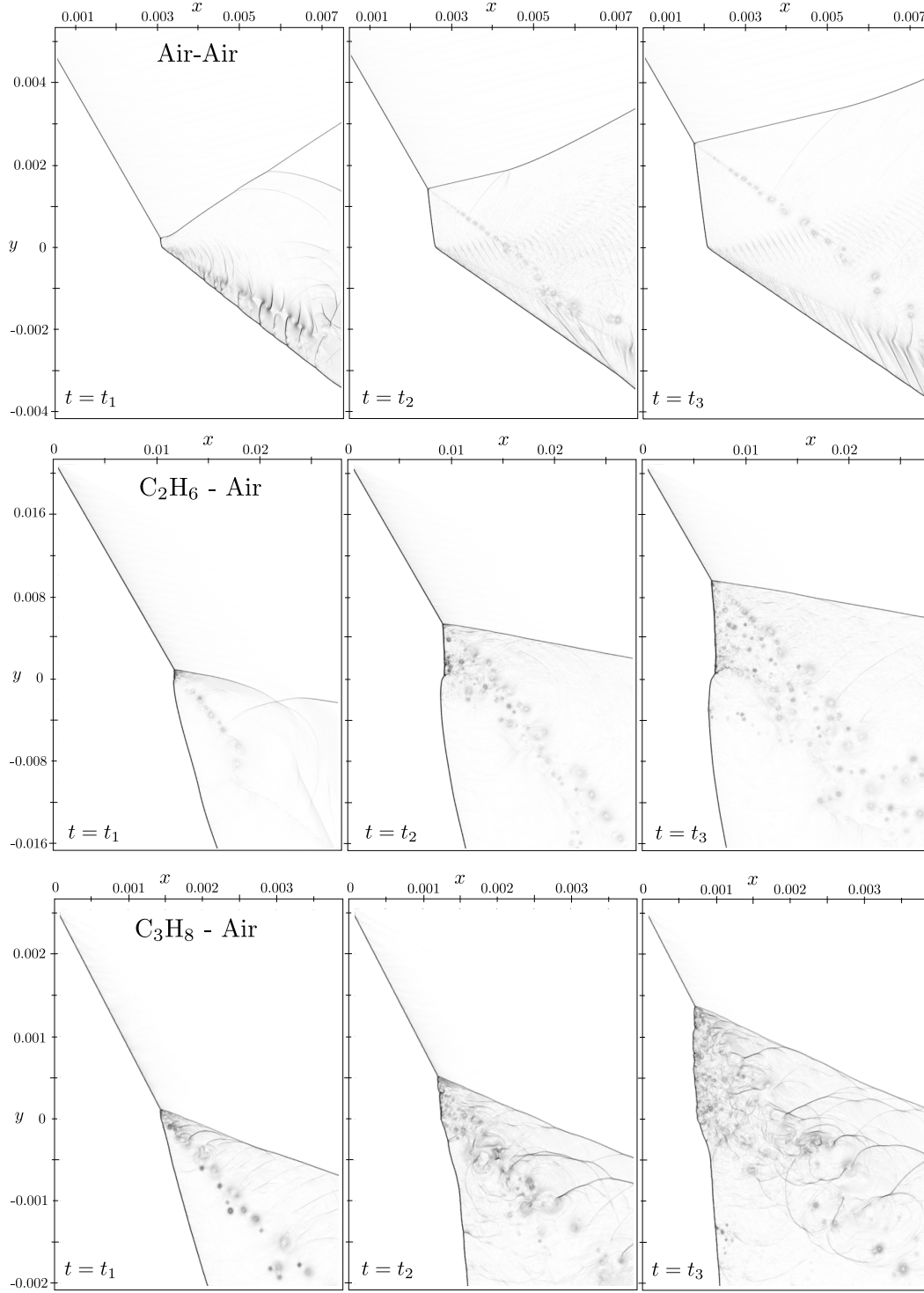
Fig. 7 Numerical schlieren of the irregular refractions with $\gamma(T, Y_\alpha)$, described in the polars of Fig. 6.

The corresponding flow fields associated to these irregular structures can be visualized by means of high-fidelity numerical simulations. The pressure and deflection mismatch provided by three straight shocks forces the evolution into an irregular configuration as shown in Fig. 7, where some snapshots of the unsteady simulations are presented. This category falls into the so-called slow-fast single Mach reflection, where the

slip line emerging from the impinging shock at $y = 0$ is accompanied by a new one that translates with the triple point and generates a vorticity layer. The only length scale available in this problem is the length of the Mach stem, which connects the triple point with the shear layer. The former grows with time while preserving its shape, as shown for consecutive time steps, and exhibiting a self-similar pseudo-steady structure. The velocity at which the triple point propagates, or the Mach stem grows, depends on the convective Mach number, as shown in [27]. The angles at the lower and upper limits of the Mach stem are given by the intersection of the blue loop with the orange and green loops, respectively. The reflected shock displays two marked angles, the self-similar segment that grows, and the original inclination that is swept away. Self-similarity is in fact a intermediate stage between the origin of the Mach stem, where it size compares to the mixing-layer thickness, and the boundary domain influences, which may enter into play by anchoring the complex-shock structure at a fixed position.

The irregular refraction of a C_2H_6-air shear layer is shown at three consecutive times in Fig. 7 (middle panel). In contrast to the previous case, and as anticipated by the polar-plot in Fig. 6(b), there is no possibility for a single Mach stem connecting the contact point at the gas interface with the backwards-moving triple point. The resulting structure comprises an incident-transmitted shock at the interface with opposite slope and a curved Mach stem that goes from the new triple point right above the contact surface to the triple point where the reflected shock emerges. The distinguished irregular refraction of a C_3H_8-air shear layer is displayed at different consecutive times in Fig. 7 (low panel). The particularly wrinkled front outcome differs from that of the air-air case, due to the completely-subsonic character of the postshock flow. The slip line produced at the triple point sheds a vortex layer which casts information that reaches the transmitted shock and, thus, produces a strong perturbation that builds up in time.

Although the above-mentioned interactions cannot be predicted with the regular analysis presented in this work, the critical limits of regular refractions in hypersonic flows can be better determined via proper consideration of the thermally-perfect modelization. To this matter, the propagation velocity of the irregular structures is directly affected by the latter, such that the further the conditions sit from the critical M_{2c} the more severe the unbalance and, therefore, the more intense the unstable evolution. Unsteadiness, which may come from expecting non-uniform conditions upstream, may also alter the limits associated to regular structures as shown in Ref. [13]. The combination of both unsteadiness and real-gas effect —representative conditions of the hypersonic regime in the upstream flow— is still to be addressed.

4 Discussion

The effects described above are usually found in high-speed flows in the presence of intense shock waves. Supersonic streams in the nearly-transonic regime may not suffer from strong variations upon consideration of constitutive relations for non-calorically perfect gases. However, the impact of these differences depends on the composition of the flow constituents in each case, where significant variations can be found for certain gases at moderate Mach numbers. The possible requisites on design geometries or conditions prescribed by flow deflection and reflected shock reach-impingement are shown here to be sharply influenced by the proper choice of modelling. Most important, regularity limits displayed in Fig. 4, either on the left or right sides, depend on the specific heat model. Narrower parametric space of regular refractions can be expected upon consideration of inaccurate calorically perfect mixtures on high-temperature or high-velocity flows. Thus, slight variations of c_p may render completely different and even unstable scenarios.

In addition, the formulation presented in Sec.2 is applicable to other configurations, as might be the case of oblique detonations, upon consideration that inner profile effects play a negligible role in the downstream base flow, i.e., the detonation front is stable. Moreover, the problem calls for external information on the chemical kinetics to predict the gas composition when thermodynamic equilibrium is achieved. The total enthalpy should be computed for the corresponding multi-species gas, but the formulation for the Rankine-Hugoniot equations remain the same. However, considering exothermic reactions may involve drastic changes in the function g with respect to the adiabatic index and the regular solution structure can be altered.

4.1 Idealized internal energy with molecular dissociation

Further physical effects should be accounted for in the limit of very strong compression, where molecular dissociation or ionization (that typically goes later) processes may utterly transform the behavior of the fluid [52–54]. The inclusion of these effects in the analysis affects the corresponding value of the heat capacity and the internal energy of the gas. Incorporation of these effects can be performed by using higher order JANAF polynomials (or more sets of the piece-wise functions) that may describe higher temperature conditions. Isolation of effects allows to write the energy equation in terms of fundamental variables. For example, let's consider the dissociation of a single-species diatomic gas. Then, the specific internal reads $\epsilon_u = (f_u/2)R_g T_u$, where f_u refers to its degrees of freedom of the diatomic molecule upstream ($f_u = 5$) and R_g to the upstream gas constant. Likewise, the internal internal downstream is $\epsilon_d = (1 - \xi_d)(f'_u/2)R_g T_d) + \xi_d f_d R_g T_d$, where $f_d = 3$ upon dissociation, but f'_u might be higher than f_u (up to 7 when the molecule behaves as pure oscillator) if vibrational modes are excited. The gas constant R_g is the one associated to the upstream diatomic stream. For example, when considering a single-species stream that undergoes partial dissociation across the shock, the corresponding energy equation reads

$$\frac{p_u}{\rho_u} + \epsilon_u + \frac{1}{2}u_{u_n}^2 = \frac{p_d}{\rho_d} + \epsilon_d + \frac{1}{2}u_{d_n}^2 + \xi_d \phi_d R_g T_d, \tag{25}$$

where $\phi_d = I_d/T_d$ is the dimensionless dissociation energy of the molecule. It is readily seen that Rankine-Hugoniot equations must be calculated with the aid of $g_u = \gamma_u = 7/5$ and

$$g_d = \frac{1 + \xi_d + \xi_d\phi_d + \dfrac{1 - \xi_d}{\gamma'_u - 1} + \dfrac{2\xi_d}{\gamma_d - 1}}{\xi_d\phi_d + \dfrac{1 - \xi_d}{\gamma'_u - 1} + \dfrac{2\xi_d}{\gamma_d - 1}} = \frac{35 - 3\xi_d + 10\xi_d\phi_d}{25 - 13\xi_d + 10\xi_d\phi_d}, \tag{26}$$

when $\gamma'_u = 7/5$ and $\gamma_d = 5/3$. It is observed that $g_d = \gamma'_u$ when $\xi_d = 0$, as expected, while $g_d = \gamma_d + 1$ for $\xi_d = 1$ and $\phi_d = 0$. The reason why $g_d \neq \gamma_d$ when dissociation is accomplished with no energy substraction stems from the fact that pressure changes by the increase of number of particles $p_d = (1 + \xi_d)R_g\rho_d T_d$. This condition must be consistently taken into account across the reflected shock. Except for very strong-shock conditions, effectively unreachable in the context chosen here, dissociation is partially accomplished and the value of $\xi_d < 1$ should be defined with the complementary Saha-Boltzmann equation for $\xi_d(T_d, \rho_d)$. For example, O_2 is dissociated at temperatures of $4,000$–$5,000$ K at ambient pressures, while N_2 may take twice this temperature [55] so weak dissociation of molecular oxygen is expected.

Equally important to note, either dissociation or combustion effects have a characteristic time that will stretch the global shock structure to dimensions comparable to the mixing-layer thickness. Therefore, the treatment of this work avoids extreme changes in the constituent matter, as expected in high-energy-density physics. Hence, the range of validity is limited to hypersonic flows, typically in aerospace applications, affected by shocks which yield temperature increases up to $T \approx 6,000$ K. However, it must be noted that the main focus is set on the effects produced by the introduction of variable thermodynamic coefficients, while simplifying the transport and production processes to an inviscid flow case. Local evaluation of the specific heat ratio as a function of the gaseous mixture composition and temperature stands on adequate resolution of heat and mass transfer processes.

4.2 Influences on the mixing layer

Although the problem formulation for the Rankine-Hugoniot equations can be applied to changes in the molecular structure trough the variable g, such as those occurring in oblique detonations, the ignition of reactive mixing layers calls for the solution of the inner interaction region. When the refracted wave is an expansion wave, the most favorable conditions for ignition to occur are right behind the shock wave [56, 57], where the shock-induced heating triggers the reaction process in a locally expanding and cooling flow. If not successful, the ignition must relay on the heat and mass transfer across the far-field mixing layer with the modified conditions through the interaction, which are found to be more favorable than those ahead of the shock [58]. The present study only considers shock refractions, so that ignition would not be restricted to the
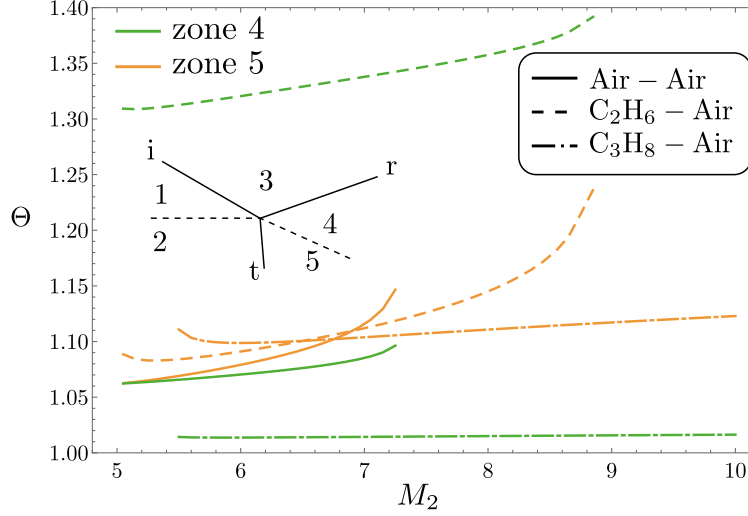
Fig. 8 Over-prediction temperature function $\Theta = T_{\gamma=\text{const.}}/T_{\gamma(T)}$ for $M_1 = 5$ and varying $M_2 > M_1$, for three different cases regarding composition of the upper stream. Green and orange lines refer to the zones behind the reflected and transmitted shocks, respectively.

vicinity of the shock within the interaction region: fluid particles go through local compression waves along its path. These compression waves collapse to form the refracted shock front outside the mixing layer. The external model, however, can only offer information about the flow conditions outside the mixing layer. As expected, since $c_p(T)$ is a monotoni cally increasing function of temperature within the range of temperatures considered, post-shock values of temperature are significantly lower with respect to the calorically-perfect configuration, either in the upper and lower streams. The overprediction in the post-shock temperature when employing a calorically-perfect gas is displayed in Fig. 8 for the cases analyzed in previous section. The factor $\Theta = T_{\gamma=\text{const.}}/T_{\gamma(T)}$ is calculated for the zones behind the reflected and transmitted shocks, corresponding to the upper and lower post-shock streams respectively. Although small, this variation can lead to much longer ignition distances in the post-shock mixing layer.

Inviscid computations are obviously not representative of an accurate momentum evolution of shear layers and their related instabilities, which would call for a three-dimensional setup in order to reproduce the real turbulent dynamics that may arise. In addition, conduction and mass diffusion effects are also hypothesized to be confined in an infinitely-thin tangential layer, which directly affects the local description of the temperature and composition fields due to mixing. The mixing-layer thickness variations would imply non-ideal flow modifications to the pictures described in the shock refraction problem, altering the local properties at the tangential discontinuities and introducing a characteristic length scale. Moreover, a detailed study of interfacial transport and mixing within the multi-species reacting shear layer that may be subject to multiple shocks interactions, transport of species and radiation, calls for multi-scale modelization coupling kinetic to meso- and macroscopic dynamics [59,60]. Nevertheless, the numerical analysis of complete turbulent, viscous and diffusive flows is out of the scope of this work, which serves to a prior understanding of the thermally-perfect considerations in shock refractions of high speed flows.

5 Conclusions

The subtle sensitivity of sudden compressions of gases to specific modeling of their enthalpy and heat capacity is explored in this work. Strong shock waves have been first presented to show the intense increases of temperature in the flow field, which are responsible for modifying the properties of the gaseous medium. That dependence has been addressed via thermally-perfect considerations, use made of JANAF polynomials in describing $c_p(T, Y_\alpha)$, and comparison with calorically-perfect gases. In order to asses the effects on the flow dynamics, one-dimensional normal shock waves are spared only to propose a canonical planar flow that may account for deflection details driven by compression effects. Particularly, the study focuses on a canonical configuration of two coflowing streams with different thermal conditions based on composition and

temperatures traversed by an oblique shock wave. This type of flow is representative of shock refractions and generates a structure of waves that is composed by the incident shock in the upper stream, which impinges in the tangential discontinuity, the transmitted shock that traverses the lower stream, and the reflected wave that arises to provide the mechanical equilibrium of the coflow downstream. Particular cases in which the reflected wave arises as a shock are selected because of the higher temperatures produced and, thus, larger expected variations on $c_p(T, Y_\alpha)$ and $\gamma(T, Y_\alpha)$.

Moreover, a modified Rankine-Hugoniot formulation is proposed by accounting for adequate jump conditions via auxiliary functions that play the part of modified Mach numbers and ratio of specific heats. This set of equations enables the theoretical calculation of post-shock conditions including thermally-perfect properties and remains valid to extend this framework for the modelling of chemically reacting layers and detonations. This feature, along with the lack of dominant scales, makes the formulation particularly useful for hydro-code verification that may involve gas molecules transformations. In this work, the theoretical predictions are demonstrated by the comparison with high-fidelity numerical simulations. It is found that under specific combinations of the streams conditions, the lack of regular configurations involving the three straight shocks mentioned above benefits from numerical simulations of the flow field to assist the theoretical analysis. These irregular scenarios have been previously reported in literature and must be considered in detail when developing technological applications of potentially unstable hypersonic flows. In this work, a description of the influence of different enthalpy modeling approaches on the critical values appearing in irregular refractions is presented.

Finally, a thorough investigation on the importance of the characterization of the thermophysical composition in high-temperature high-velocity flows evidences the failure of disregarding the variations of heat capacity with temperature and composition. Over-predictions in the temperature field outside the postshock mixing layer, which may reach up to 40%, are obtained when heat capacity is assumed to be constant. The examples provided in this study are used to demonstrate the extreme variations in the flow that may be expected upon incorporation of the selected thermal physics.

Acknowledgements

A Numerical implementation

Further details on the implementation of the flow solver CREAMS are provided in this appendix. It consists of a high-fidelity fluid dynamics code for fully compressible Navier-Stokes equations. The scheme is a spatial seventh-order accurate WENO and a third-order total variation diminishing Runge-Kutta [51].

The system of equations that describe a three-dimensional, unsteady, compressible and viscous gas mixture composed of N reactive species, where external forces and radiation are neglected, is expressed as

$$\frac{\partial \rho}{\partial t} + \frac{\partial \rho u_j}{\partial x_j} = 0, \tag{27}$$

$$\frac{\partial \rho u_i}{\partial t} + \frac{\partial (\rho u_i u_j + p)}{\partial x_j} = \frac{\partial \rho \tau_{ij}}{\partial x_j}, \quad i = 1, 2, 3, \tag{28}$$

$$\frac{\partial \rho e_t}{\partial t} + \frac{\partial (\rho e_t + p) u_j}{\partial x_j} = \frac{\partial \rho \tau_{ij} u_i}{\partial x_j} - \frac{\partial q}{\partial x_j}, \tag{29}$$

$$\frac{\partial \rho Y_\alpha}{\partial t} + \frac{\partial \rho Y_\alpha u_j}{\partial x_j} = -\frac{\partial \rho Y_\alpha V_{\alpha j}}{\partial x_j}, \quad \alpha = 1, \ldots, N. \tag{30}$$

The pressure of the gas mixture is given by p, which is related to the density ρ and temperature T of the mixture via the equation of state of a perfect gas, i.e., $p = \rho R T / W$, where $R = 8.314\,\text{J/molK}$ is

the universal constant for perfect gases. To close this system of equations in thermodynamics terms, both constant and variable specific heat ratios are considered. What is more, non-reactive inviscid computations without heat conduction and mass diffusion of species are performed with the intention of reproducing ideal-flow theoretical conditions and isolating the thermally-perfect gas effects. Therefore, the r.h.s. terms in (28)–(30) are set to zero for the simulations carried out.

The numerical setup used to compute a two-dimensional mixing layers follows previous works based on temporally-developing [61,62] and spatially-developing [63–65,27] shear layers. The flow is initialized using a hyperbolic tangent for the velocity profile

$$u_1 = \frac{U_1 + U_2}{2} + \frac{U_1 - U_2}{2} \tanh\left(\frac{2x_2}{\delta_{\omega,0}}\right), \tag{31}$$

where U_1 and U_2 are the mean streamwise velocities of the top and bottom streams, respectively, and $\delta_{\omega,0}$ is the initial vorticity thickness of the shear layer

$$\delta_{\omega,0} = \frac{U_1 - U_2}{|\partial \langle u_1 \rangle_{\mathrm{f}}/\partial x_2|_{\max,x_1=0}}, \tag{32}$$

where brackets indicate Reynolds averaged quantities and the index "f" is utilized for Favre averaged quantities. The initial vorticity thickness controls the amount of initial dissipation between the two streams and has an associated Reynolds number

$$\mathrm{Re}_{\omega,0} = \frac{(\rho_1 + \rho_2)|U_1 - U_2|\delta_{\omega,0}}{\mu_1 + \mu_2} \tag{33}$$

that is set to $\mathrm{Re}_{\omega,0} = 640$ in this work following [61,64,65]. This condition provides $\delta_{\omega,0} = 2.79 \cdot 10^{-5}\,\mathrm{m}$ (air-air shear layer), $1.41 \cdot 10^{-4}\,\mathrm{m}$ (ethane-air mixing layer) and $1.74 \cdot 10^{-5}\,\mathrm{m}$ (propane-air mixing layer), which are employed to define the grid size ($\Delta x \approx 0.168\delta_{\omega,0}$ for a typical DNS). Although the definition of a vorticity thickness is not compatible with the idealization of the flow, for which the hyperbolic tangent profile would asymptotically degenerate into a step function, $\delta_{\omega,0} \neq 0$ is still employed for the following two reasons. Firstly, it characterizes the numerical estimated grid size in the absence of diffusion terms in the conservation equations. Secondly, it was previously shown that the choice of $\delta_{\omega,0} \neq 0$ at the inlet boundary does not fail to reproduce the theoretical inviscid flow field [27].

The computational domain is bounded by an area measuring roughly $800\,\delta_{\omega,0} \times 800\,\delta_{\omega,0}$. The region of interest is placed at the top left corner and covers a squared region of dimensions $300\,\delta_{\omega,0} \times 300\,\delta_{\omega,0}$, which provides large span for the information to reach the outflow boundaries. This primary area is discretized with a constant grid size $\Delta x = 0.25\,\delta_{\omega,0}$ whilst the rest of the computational domain is progressively meshed with a linear stretch towards the exit with a constant factor of 5%. The boundary conditions that reproduce the mixing or shear layer problem hold a supersonic inlet where Dirichlet conditions are imposed for pressure, temperature and mixture composition at the left boundary, together with the velocity profile of eq. (31). In addition, the top boundary includes Rankine-Hugoniot jump conditions for an ideal gas mixture. Furthermore, non-reflecting conditions are applied at the far bottom and right boundaries. Finally, a constant CFL number of 0.5 is selected for time integration.

As already mentioned, inviscid numerical simulations have been carried out in this work with the aim of reproducing ideal-flow theoretical conditions. We expect that viscous effects will only play a significant role in very specific areas (e.g. regions with high levels of turbulence that may appear ahead of the shock impingement, but whose characteristic scales are smaller than that of the mixing-layer thickness [3]). Viscous effects may be also important in determining the vortex roll-up pattern generated downstream, specially in irregular configurations where additional evolutionary scales are present. Vibrational relaxation, on the other hand, may exhibit large-scale effects related to the regular configuration limits [14]. To demonstrate that our inviscid simulations do retain the same behaviour observed in real-flows of shear and mixing layers under similar conditions, we have conducted the reciprocal viscous simulations. Figure 9 shows the evolution of the transmitted shock angle with the Mach number of the lower stream for a shear layer of air impinged with a shock wave at 50°. The flow is assumed to be either inviscid or viscous using both a simplified and a detailed description of the corresponding transport terms which are found at the r.h.s. of eqs. (27)-(30). Without getting into too much detail, the simplified description relies upon a mixture-averaged formulation based
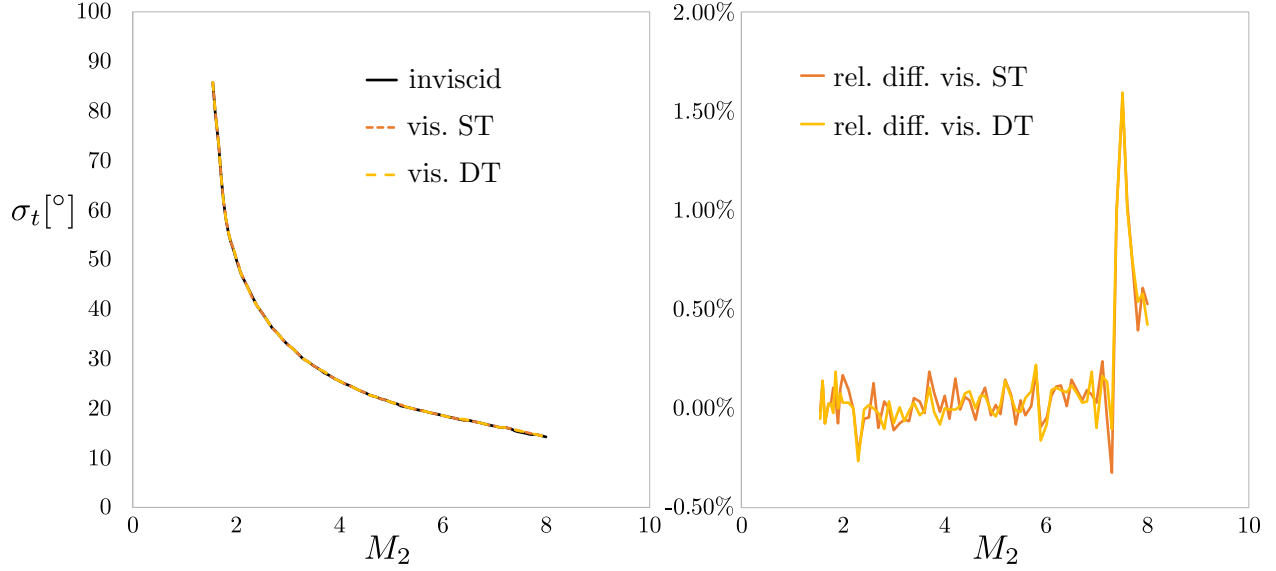
Fig. 9 Numerical-simulation values for the transmitted shock angle σ_t as a function of the lower stream Mach number M_2. Computations made for air-air mixing layers with $M_1 = 2$, $\sigma_i = 50°$ and variable specific heat $c_p(T)$. The gas mixture is treated as an inviscid flow as well as a viscous flow using both simplified (ST) and detailed (DT) transport models. Relative differences of transmitted shock angle under the two viscous simulations with respect to the inviscid case.

on the Hirschfelder & Curtiss approximation whilst the detailed description takes into account differential diffusion, Soret, Dufour and bulk viscosity effects [51]. It can be readily seen from this figure that the three simulations fall within the same curve as expected. A much closer inspection at the transmitted shock angle relative differences between the two viscous cases with respect to the inviscid one, see Fig. 9, reveals that these differences are well below $\pm 0.5\%$ and suddenly spike at $M_2 \approx 7.5$. After this, the relative errors reduce to roughly 0.5% but, unfortunately, the lack of additional data beyond $M_2 = 8$ does not allow us to estimate the trend of the relative error. We believe that the relative error will continue to increase as the value of the transmitted angle diminishes. Indeed, the algorithm used to compute this angle must identify two sufficiently distant points along the transmitted shock: while the first point is always very close to the triple point, the second one might fall outside the squared region of interest (featuring a small grid size) for flattened transmitted shocks thus deteriorating the accuracy of the measurement.

References

1. Urzay, J.: Supersonic combustion in air-breathing propulsion systems for hypersonic flight. Annual Review of Fluid Mechanics **50**, 593–627 (2018). DOI https://doi.org/10.1146/annurev-fluid-122316-045217
2. Candler, G.V.: Rate effects in hypersonic flows. Annual Review of Fluid Mechanics **51**, 379–402 (2019). DOI https://doi.org/10.1146/annurev-fluid-010518-040258
3. Ma, K., Li, J., Li, Q., Liu, Y., Li, X., Ma, D., Ao, W.: Evolution characteristics of subsonic-supersonic mixing layer impinged by shock waves. Aerospace Science and Technology **106**, 106150 (2020). DOI https://doi.org/10.1016/j.ast.2020.106150
4. Andreopoulos, Y., Agui, J.H., Briassulis, G.: Shock wave-turbulence interactions. Annual Review of Fluid Mechanics **32**(1), 309–345 (2000). DOI https://doi.org/10.1146/annurev.fluid.32.1.309
5. Cook, A.W., Cabot, W.H.: Hyperviscosity for shock-turbulence interactions. Journal of Computational Physics **203**(2), 379–385 (2005). DOI https://doi.org/10.1016/j.jcp.2004.09.011
6. Wouchuk, J., Huete, C., Velikovich, A.: Analytical linear theory for the interaction of a planar shock wave with an isotropic turbulent vorticity field. Physical Review E **79**(6), 066315 (2009). DOI https://doi.org/10.1103/PhysRevE.79.066315
7. Ryu, J., Livescu, D.: Turbulence structure behind the shock in canonical shock-vortical turbulence interaction. Journal of Fluid Mechanics **756** (2014). DOI https://doi.org/10.1017/jfm.2014.477
8. Livescu, D.: Turbulence with large thermal and compositional density variations. Annual Review of Fluid Mechanics **52**(1), 309–341 (2020). DOI https://doi.org/10.1146/annurev-fluid-010719-060114
9. Nishihara, K., Wouchuk, J.G., Matsuoka, C., Ishizaki, R., Zhakhovsky, V.V.: Richtmyer-Meshkov instability: theory of linear and nonlinear evolution. Philosophical Transactions: Mathematical, Physical and Engineering Sciences **368**(1916), 1769–1807 (2010). URL http://www.jstor.org/stable/25663341
10. Stanic, M., Stellingwerf, R.F., Cassibry, J.T., Abarzhi, S.I.: Scale coupling in Richtmyer-Meshkov flows induced by strong shocks. Physics of Plasmas **19**(8), 082706 (2012). DOI 10.1063/1.4744986

11. Dell, Z., Pandian, A., Bhowmick, A., Swisher, N., Stanic, M., Stellingwerf, R., Abarzhi, S.: Maximum initial growth-rate of strong-shock-driven Richtmyer-Meshkov instability. Physics of Plasmas **24**(9), 090702 (2017). DOI https://doi.org/10.1063/1.4986903

12. Lin, J., Bai, C.Y., Wu, Z.N.: Study of asymmetrical shock wave reflection in steady supersonic flow. Journal of Fluid Mechanics **864**, 848–875 (2019). DOI 10.1017/jfm.2019.18

13. Laguarda, L., Hickel, S., Schrijer, F.F.J., van Oudheusden, B.W.: Dynamics of unsteady asymmetric shock interactions. Journal of Fluid Mechanics **888**, A18 (2020). DOI https://doi.org/10.1017/jfm.2020.28

14. Glaz, H.M., Colella, P., Glass, I., Deschambault, R.: A numerical study of oblique shock-wave reflections with experimental comparisons. Proceedings of the Royal Society of London. A. Mathematical and Physical Sciences **398**(1814), 117–140 (1985). DOI https://doi.org/10.1098/rspa.1985.0028

15. Dewey, J., McMillin, D.: Observation and analysis of the Dach reflection of weak uniform plane shock waves. Part 1. Observations. Journal of Fluid Mechanics **152**, 49–66 (1985). DOI https://doi.org/10.1017/S0022112085000568

16. Dewey, J., McMillin, D.: Observation and analysis of the Mach reflection of weak uniform plane shock waves. Part 2. Analysis. Journal of Fluid Mechanics **152**, 67–81 (1985). DOI https://doi.org/10.1017/S002211208500057X

17. Ben-Dor, G.: Shock wave reflection phenomena, vol. 2. Springer (2007). DOI https://doi.org/10.1007/978-3-540-71382-1

18. Lighthill, M.J.: On boundary layers and upstream influence II. Supersonic flows without separation. Proceedings of the Royal Society of London. Series A. Mathematical and Physical Sciences **217**(1131), 478–507 (1953). DOI https://doi.org/10.1098/rspa.1953.0075

19. Henderson, L.: The reflexion of a shock wave at a rigid wall in the presence of a boundary layer. Journal of Fluid Mechanics **30**(4), 699–722 (1967). DOI https://doi.org/10.1017/S0022112067001715

20. Stewartson, K., Williams, P.: Self-induced separation. Proceedings of the Royal Society of London A. Mathematical and Physical Sciences **312**(1509), 181–206 (1969). DOI https://doi.org/10.1098/rspa.1969.0148

21. Matheis, J., Hickel, S.: On the transition between regular and irregular shock patterns of shock-wave/boundary-layer interactions. Journal of Fluid Mechanics **776**, 200–234 (2015). DOI https://doi.org/10.1017/jfm.2015.319

22. Adler, M.C., Gaitonde, D.V.: Dynamic linear response of a shock/turbulent-boundary-layer interaction using constrained perturbations. Journal of Fluid Mechanics **840**, 291–341 (2018). DOI https://doi.org/10.1017/jfm.2018.70

23. Dupont, P., Piponniau, S., Dussauge, J.: Compressible mixing layer in shock-induced separation. Journal of Fluid Mechanics **863**, 620–643 (2019). DOI https://doi.org/10.1017/jfm.2018.987

24. Fu, L., Karp, M., BoseShow, S.T., Moin, P., Urzay, J.: Shock-induced heating and transition to turbulence in a hypersonic boundary layer. Journal of Fluid Mechanics **(in press)** (2021). DOI pending

25. Henderson, L.: The refraction of a plane shock wave at a gas interface. Journal of Fluid Mechanics **26**(3), 607–637 (1966). DOI https://doi.org/10.1017/S0022112066001435

26. Estruch-Samper, D., Chandola, G.: Separated shear layer effect on shock-wave/turbulent-boundary-layer interaction unsteadiness. Journal of Fluid Mechanics **848**, 154–192 (2018). DOI https://doi.org/10.1017/jfm.2018.350

27. Martínez-Ruiz, D., Huete, C., Martínez-Ferrer, P.J., Mira, D.: Irregular self-similar configurations of shock-wave impingement on shear layers. Journal of Fluid Mechanics **872**, 889–927 (2019). DOI https://doi.org/10.1017/jfm.2019.336

28. Mach, E.: Uber den Verlauf von Funkenwellen in der Ebene und im Raume. Sitzungsberichte der kaiserlichen Akademie der Wissenschaften in Wien **78**, 819–838 (1878)

29. Hornung, H.: Regular and Mach reflection of shock waves. Annual Review of Fluid Mechanics **18**(1), 33–58 (1986). DOI https://doi.org/10.1146/annurev.fl.18.010186.000341

30. Riley, N.: Interaction of a shock wave with a mixing region. Journal of Fluid Mechanics **7**(3), 321–339 (1960). DOI https://doi.org/10.1017/S0022112060000116

31. Huete, C., Urzay, J., Sánchez, A.L., Williams, F.A.: Weak-shock interactions with transonic laminar mixing layers of fuels for high-speed propulsion. AIAA Journal **54**(3), 966–979 (2016). DOI https://doi.org/10.2514/1.J054419

32. Rikanati, A., Sadot, O., Ben-Dor, G., Shvarts, D., Kuribayashi, T., Takayama, K.: Shock-wave Mach-reflection slip-stream instability: a secondary small-scale turbulent mixing phenomenon. Physical Review Letters **96**(17), 174503 (2006). DOI https://doi.org/10.1103/PhysRevLett.96.174503

33. Rubidge, S., Skews, B.: Shear-layer instability in the Mach reflection of shock waves. Shock Waves **24**(5), 479–488 (2014). DOI https://doi.org/10.1007/s00193-014-0515-6

34. Patel, A., Singh, M.: Exact solution of shock wave structure in a non-ideal gas under constant and variable coefficient of viscosity and heat conductivity. Shock Waves **29**(3), 427–439 (2019). DOI https://doi.org/10.1007/s00193-018-0855-8

35. Singh, M., Patel, A.: Shock wave structure in a non-ideal gas under temperature and density-dependent viscosity and heat conduction. Theoretical and Computational Fluid Dynamics **33**(6), 537–559 (2019). DOI https://doi.org/10.1007/s00162-019-00505-y

36. Liu, H., Chen, H., Zhang, B., Liu, H.: Effects of Mach number on non-Rankine-Hugoniot shock zone of Mach reflection. Journal of Spacecraft and Rockets **56**(3), 761–770 (2019). DOI https://doi.org/10.2514/1.A34251

37. Shi, X., Zhu, Y., Yang, J., Luo, X.: Mach stem deformation in pseudo-steady shock wave reflections. Journal of Fluid Mechanics **861**, 407–421 (2019). DOI https://doi.org/10.1017/jfm.2018.920

38. Meyerhoff, L.: An extension of the theory of the one-dimensional shock-wave structure. Journal of the Aeronautical Sciences **17**(12), 775–786 (1950). DOI https://doi.org/10.2514/8.1806

39. Kestin, J.: The influence of the temperature variation of the specific heats of air in shock-wave calculations. Journal of the Aeronautical Sciences **18**(5), 351–353 (1951). DOI https://doi.org/10.2514/8.1953

40. Orudzhaliev, E.: On the theory of shock waves in the dynamics of a real gas. International Journal of Heat and Mass Transfer **6**(11), 935–940 (1963). DOI https://doi.org/10.1016/0017-9310(63)90048-6

41. John, B., Kulkarni, V.N., Natarajan, G.: Shock wave boundary layer interactions in hypersonic flows. International Journal of Heat and Mass Transfer **70**, 81–90 (2014). DOI https://doi.org/10.1016/j.ijheatmasstransfer.2013.10.072

42. Ben-Dor, G., Glass, I.I.: Domains and boundaries of non-stationary oblique shock-wave reflexions. 1. Diatomic gas. Journal of Fluid Mechanics **92**(3), 459–496 (1979). DOI https://doi.org/10.1017/S0022112079000732

43. Ben-Dor, G., Glass, I.I.: Domains and boundaries of non-stationary oblique shock-wave reflexions. 2. Monatomic gas. Journal of Fluid Mechanics **96**(4), 735–756 (1980). DOI https://doi.org/10.1017/S0022112080002339

44. Deschambault, R., Glass, I.: An update on non-stationary oblique shock-wave reflections: Actual isopycnics and numerical experiments. Journal of Fluid Mechanics **131**, 27–57 (1983). DOI https://doi.org/10.1017/S0022112083001226

45. Henderson, L., Macpherson, A.: On the irregular refraction of a plane shock wave at a Mach number interface. Journal of Fluid Mechanics **32**(1), 185–202 (1968). DOI https://doi.org/10.1017/S0022112068000650

46. Abd-El-Fattah, A., Henderson, L.F., Lozzi, A.: Precursor shock waves at a slow-fast gas interface. Journal of Fluid Mechanics **76**(1), 157–176 (1976). DOI https://doi.org/10.1017/S0022112076003182

47. Abd-El-Fattah, A., Henderson, L.: Shock waves at a fast-slow gas interface. Journal of Fluid Mechanics **86**(1), 15–32 (1978). DOI https://doi.org/10.1017/S0022112078000981

48. Abd-El-Fattah, A., Henderson, L.: Shock waves at a slow-fast gas interface. Journal of Fluid Mechanics **89**(1), 79–95 (1978). DOI https://doi.org/10.1017/S0022112078002475

49. Ahlborn, B.: A simple iteration for shock wave calculations with the enthalpy coefficient. Canadian Journal of Physics **53**(10), 976–979 (1975). DOI https://doi.org/10.1139/p75-124

50. Chase Jr., M.W., Curnutt, J.L., Downey Jr., J.R., McDonald, R.A., Syverud, A.N., Valenzuela, E.A.: JANAF thermochemical tables, 1982 supplement. Journal of Physical and Chemical Reference Data **11**(695) (1982). DOI https://doi.org/10.1063/1.555666

51. Ferrer, P.J.M., Buttay, R., Lehnasch, G., Mura, A.: A detailed verification procedure for compressible reactive multicomponent Navier-Stokes solvers. Computers & Fluids **89**, 88–110 (2014). DOI https://doi.org/10.1016/j.compfluid.2013.10.014

52. Kuo, Y.: Dissociation effects in hypersonic viscous flows. Journal of the Aeronautical Sciences **24**(5), 345–350 (1957). DOI https://doi.org/10.2514/8.3847

53. Treanor, C.E., Marrone, P.V.: Effect of dissociation on the rate of vibrational relaxation. The Physics of Fluids **5**(9), 1022–1026 (1962). DOI https://doi.org/10.1063/1.1724467

54. Josyula, E., Bailey, W.F.: Vibration-dissociation coupling using master equations in nonequilibrium hypersonic blunt-body flow. Journal of Thermophysics and Heat Transfer **15**(2), 157–167 (2001). DOI https://doi.org/10.2514/2.6604

55. Bauer, E.: Physics of high-temperature air. Part 1. Basics. Final report, October 1987-December 1988. Tech. rep., Institute for Defense Analyses, Alexandria, VA (USA) (1990). DOI https://doi.org/10.21236/ADA224584

56. Huete, C., Sánchez, A.L., Williams, F.A., Urzay, J.: Diffusion-flame ignition by shock-wave impingement on a supersonic mixing layer. Journal of Fluid Mechanics **784**, 74–108 (2015). DOI https://doi.org/10.1017/jfm.2015.585

57. Huete, C., Sánchez, A.L., Williams, F.A.: Diffusion-flame ignition by shock-wave impingement on a hydrogen–air supersonic mixing layer. Journal of Propulsion and Power **33**(1), 256–263 (2017). DOI https://doi.org/10.2514/1.B36236

58. Martínez-Ruiz, D., Huete, C., Sánchez, A.L., Williams, F.A.: Interaction of oblique shocks and laminar shear layers. AIAA Journal **56**(3), 1023–1030 (2018). DOI https://doi.org/10.2514/1.J056302

59. Abarzhi, S.I., Goddard, W.A.: Interfaces and mixing: Nonequilibrium transport across the scales. Proceedings of the National Academy of Sciences **116**(37), 18171–18174 (2019). DOI https://doi.org/10.1073/pnas.1818855116

60. Ilyin, D.V., Goddard III, W.A., Abarzhi, S.I.: Inertial dynamics of an interface with interfacial mass flux: Stability and flow fields' structure, inertial stabilization mechanism, degeneracy of Landau's solution, effect of energy fluctuations, and chemistry-induced instabilities. Physics of Fluids **32**(8), 082105 (2020). DOI https://doi.org/10.1063/5.0013165

61. Pantano, C., Sarkar, S.: A study of compressibility effects in the high-speed turbulent shear layer using direct simulation. Journal of Fluid Mechanics **451**, 329–371 (2002). DOI https://doi.org/10.1017/S0022112001006978

62. Mahle, I., Foysi, H., Sarkar, S., Friedrich, R.: On the turbulence structure in inert and reacting compressible mixing layers. Journal of Fluid Mechanics **593**, 171–180 (2007). DOI https://doi.org/10.1017/S002211200700891

63. Stanley, S., Sarkar, S.: Simulations of spatially developing two-dimensional shear layers and jets. Theoretical and Computational Fluid Dynamics **9**(2), 121–147 (1997). DOI https://doi.org/10.1007/s001620050036

64. Fu, S., Li, Q.: Numerical simulation of compressible mixing layers. International Journal of Heat and Fluid Flow **27**(5), 895–901 (2006). DOI https://doi.org/10.1016/j.ijheatfluidflow.2006.03.028

65. Ferrer, P.J.M., Lehnasch, G., Mura, A.: Compressibility and heat release effects in high-speed reactive mixing layers i.: Growth rates and turbulence characteristics. Combustion and Flame **180**, 284–303 (2017). DOI https://doi.org/10.1016/j.combustflame.2016.09.008